



Ultra-broadband ptychography for dispersive samples

Received: 1 January 2025

Accepted: 19 June 2025

Published online: 01 July 2025

Check for updates

Huixiang Lin^①, Angyi Lin¹, Xiaoyu Jin¹, Kui Li², Jin Niu³, Jie Li³, Xiaoshi Zhang², Tao Liu¹, Wenhui Xu⁴ & Fucai Zhang^①✉

X-ray ptychography has emerged as a powerful imaging tool on X-ray synchrotron facilities. Implementation of ptychography on laboratory-scale X-ray sources has largely been hindered by their poor temporal coherence and low flux. Here we propose an ultra-broadband method incorporating structured illumination to enhance the robustness of ptychography to broadband sources. Different from other methods, our ultra-broadband ptychography method enables imaging of dispersive samples without prior knowledge of light spectra. A 60% bandwidth light source and a high harmonic extreme ultraviolet source were used to validate our method. Moreover, our method demonstrates precise quantitative phase imaging capabilities. The proposed method will significantly advance the implementation of ptychography on laboratory-scale broadband X-ray sources and widen its applications in biomedicine and materials science.

The growing demand for precise characterization of materials, non-destructive inspection of semiconductor devices, and high-resolution imaging of biological specimens in their native states has highlighted the critical importance of X-ray imaging, which provides unmatched capabilities for deep penetration and nanoscale resolution of complex internal structures. Due to the advantages of not requiring high-quality imaging lenses and having a spatial resolution theoretically limited only by the illumination wavelength, ptychography has become one of the mainstream methods in X-ray imaging^{1–3}. Specifically, it is a scanning coherent diffraction imaging (CDI) method that increases data redundancy through partially overlapping sample scans and achieves high-quality quantitative phase imaging using specific phase retrieval algorithms^{4,5}. Consequently, X-ray ptychography has been widely applied in nanoscale structural measurement of biological and material samples^{6,7}, spatial mapping of chemical compositions⁸, and non-destructive measurement of integrated circuit architectures and surface morphologies^{9,10}. Due to the demands for high-flux and high-coherence illumination, these experiments have mostly been restricted to synchrotron facilities.

In recent years, technological advancements in laboratory X-ray sources, particularly liquid metal jet X-ray sources and high harmonic

generation (HHG) extreme ultraviolet (EUV) sources, have significantly increased their brightness, making them increasingly suitable for lensless imaging techniques^{11–16}. However, laboratory X-ray sources typically have a relatively large bandwidth, requiring monochromatic filtering to meet the fully coherent model assumptions of ptychography¹⁷. This process significantly reduces the usable flux of the source, thereby affecting the dose-limited spatial resolution and image quality^{18,19}. Therefore, compensating for the effects of broadband sources through algorithms and directly using unfiltered high-flux illumination for imaging is an effective approach.

Recently, several numerical methods have been proposed to enhance the robustness of CDI to broadband sources. A multi-wavelength reconstruction algorithm was developed for CDI experiments utilizing a laboratory-scale high-harmonic-generation (HHG) source, which scales the far-field diffraction pattern of the central wavelength to estimate the intensities of other harmonics and performs incoherent superposition to construct a polychromatic reconstruction model²⁰. Subsequently, this method was further developed into PolyCDI, which enables imaging with continuous-spectrum sources, and was demonstrated using a synchrotron X-ray source, achieving a 60-fold reduction in exposure time compared to monochromatic

¹State Key Laboratory of Quantum Functional Materials, Department of Electronic and Electrical Engineering, Southern University of Science and Technology, Shenzhen, China. ²School of Physics and Astronomy, Yunnan University, Kunming, Yunnan, China. ³Aerospace Information Research Institute, Chinese Academy of Sciences, Beijing, China. ⁴Paul Scherrer Institut, Villigen PSI, Switzerland. ✉e-mail: zhangfc@sustech.edu.cn

CDI²¹. Moreover, a model incorporating the simultaneous propagation of multiple wavelengths was introduced into the reconstruction algorithm, enhancing robustness to broadband sources while enabling the simultaneous reconstruction of responses at multiple wavelengths^{22–26}. In addition, the two-step CDI method, which extracts single-wavelength diffraction patterns from polychromatic data for traditional CDI reconstruction, has been validated using discrete high-harmonic sources²⁷. With advancements in algorithms, numerical monochromatization methods employ regularized inversion to extract monochromatic data from continuous-spectrum datasets, with a bandwidth of up to 11%²⁸. Subsequently, monochromatization methods were further optimized to handle broader bandwidths of sources^{29–31}. The above methods are primarily based on the theory of coherent mode decomposition³², relying on known spectral distributions as prior knowledge for incoherent superposition of diffraction patterns and assuming that the sample is non-dispersive, so that diffraction patterns at different wavelengths are scaled versions of each other²¹.

In practical imaging applications, dispersive samples with complex amplitude information are often encountered, where diffraction patterns are no longer simple scaled versions of each other. Moreover, in the X-ray regime, many elements exhibit absorption edge characteristics, directly causing significant changes in the spectral distribution at the detector. The latest broadband diffraction imaging method can obtain the spectral information through numerical calculations, enabling more precise numerical monochromatization³⁰. Although this method partially compensates for spectral variations arising from sample absorption and detector quantum efficiency, the spectral variations of complex dispersive samples in each scanning region of ptychography are unable to be determined in advance. An alternative partial-coherent-model distinct from the coherent mode decomposition is the convolution model, which offers potential solutions to these challenges. This model represents low-coherence diffraction patterns by convolving a kernel encapsulating coherence information with fully coherent diffraction patterns^{33,34}. By introducing a blind deconvolution step into the iterative reconstruction process of

the algorithm, the blur kernel can be progressively updated, thereby compensating for the effects of low spatial or temporal coherence^{35–37}.

In this work, we propose an ultra-broadband ptychography method that incorporates the broadband convolution model, enabling imaging of dispersive samples without requiring prior spectral information. Our method uses a multi-kernel iterative deconvolution update strategy called joint deconvolution algorithm, in combination with structured illumination provided by a phase mask in the data acquisition, greatly enhancing the bandwidth robustness and reconstruction quality of our method. We highlight the key reasons for the failure of current methods for dispersive samples and demonstrate a significantly improved approach for handling cases where different regions of the sample exhibit varying spectral responses. The proposed ultra-broadband method is in principle applicable to broadband sources across any wavelength range, including laboratory-scale X-ray and HHG EUV sources.

Results

Ultra-broadband ptychography via convolution model

As illustrated in the schematic diagram in Fig. 1, in far-field ptychography, the broadband illumination passes through a structured aperture to form a probe, which subsequently scans across the sample plane orthogonal to its propagation direction. The illuminated regions at adjacent scan positions \mathbf{r}_j exhibit partial overlap, ensuring sufficient redundancy for phase retrieval. The exit waves propagate through free space to the detector plane, where the far-field partially coherent diffraction patterns I_j^{coh} are recorded. Here the I_j^{coh} can be represented using the broadband convolution model, which is the convolution of a coherent diffraction pattern I_j^{coh} with a blur kernel h_j containing coherence information^{33,34},

$$I_j^{coh}(\mathbf{q}) = I_j^{coh}(\mathbf{q}) \otimes h_j(\mathbf{q}) \quad (1)$$

where \mathbf{q} is a position vector in reciprocal space and \otimes represents the convolution operator. Therefore, the robustness of existing fully coherent iterative algorithms can be enhanced for broadband sources

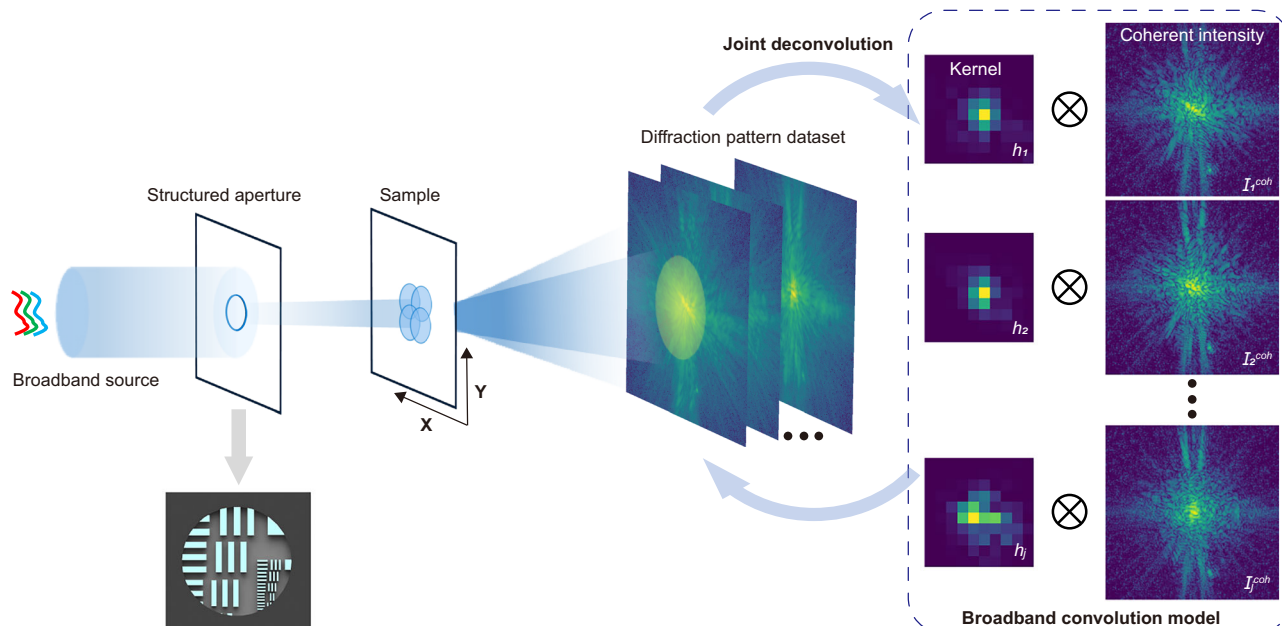


Fig. 1 | Principle of ultra-broadband ptychography. The broadband source passes through a phase-type structured aperture, forming a structured probe on the sample for two-dimensional scanning. Then, the transmitted wave propagates through free space to the detector plane, where the broadband far-field diffraction

pattern dataset is recorded. The broadband diffraction intensity can be expressed in the form of a convolution between the coherent diffraction intensity and the kernel containing coherence information.

by incorporating a blurring kernel, which is obtained through blind deconvolution within the phase retrieval process^{36,37}.

To better fit the measured polychromatic diffraction patterns, we introduced the broadband convolution model into the reconstruction process. As shown in Fig. 1, each diffraction pattern at different scanning positions is assigned its own blurring kernel, rather than sharing a common kernel across all. The kernels are updated throughout the iterative process, which are obtained via blind deconvolution from the measured broadband patterns and the calculated coherent patterns. Here, we employed a joint deconvolution algorithm, inspired by the iterative probe update strategy used in the extended ptychographic iterative engine (ePIE)³⁸. The blurring kernel obtained from the previous scan position is used as the initial value for the deconvolution iterations at the next scan position, thereby further improving the accuracy of the retrieved kernel (detailed in Methods). This strategy, based on the overall stable coherence of the system, leverages the kernel from the preceding scan position as the initial input, effectively utilizing the data redundancy in ptychography to enhance the convergence of the deconvolution algorithm. Subsequent iterative updates for each kernel further compensate for minor decoherence effects arising from system instabilities or sample movements.

Since the kernels of FT-MCF (Fourier transform of the normalized mutual coherence function) are iteratively updated during the reconstruction process, our ultra-broadband ptychography method does not require pre-measured spectral weight distributions as prior information, significantly simplifying broadband imaging experiments. Furthermore, it eliminates the need for the non-dispersive sample assumption, enabling the imaging of samples with absorption edges or significant dispersive effects within the spectral range, thereby greatly expanding the practical applicability. Moreover, we incorporated a phase-type structured mask into the system to generate structured illumination. Although structured light generated by amplitude masks has been proven effective in compensating for decoherence effects^{39,40}, such masks significantly reduce the photon flux. Hence, we integrate the proposed retrieval algorithm with the phase-type structured illumination, significantly enhancing the performance of the broadband imaging while substantially reducing photon flux loss caused by absorption.

Broadband imaging of biological specimens

The capability for high-quality imaging of biological specimens, which are among the most common complex amplitude samples, is crucial for the practical applicability of ultra-broadband ptychography. To validate the feasibility of our method, we initially conducted an optical experiment on an ant utilizing a source with a bandwidth $\Delta\lambda/\lambda = 60\%$, where λ is the central wavelength and $\Delta\lambda$ is the full width at half maximum (FWHM). Note that all bandwidths mentioned subsequently are defined as the FWHM. We built a proof-of-principle ptychographic imaging system as shown in Fig. 2a. A supercontinuum source with a full width at half maximum (FWHM) of 420 nm (SC-5, YSL Photonics) was used as the source for ultra-broadband illumination, the corresponding spectral distribution is shown in Fig. 2a. However, this spectrum is merely used for demonstration purposes. After collimation and spatial filtering, the broadband illumination passes through a pinhole to form a light probe on the ant specimen. The optical microscope image of the ant is also illustrated in Fig. 2a. Notably, the depth of field under our system configuration is estimated to be $\sim 230 \mu\text{m}$, allowing all the samples we used to be reasonably treated as two-dimensional objects under the projection approximation. Here, a phase-type USAF resolution target (Edmund Optics) was placed at the pinhole plane to generate structured illumination. Subsequently, the far-field diffraction patterns of the exit wave of sample were collected by the detector, as shown in Fig. 2a.

The proposed ultra-broadband ptychography method is developed by integrating a broadband convolution model and a joint

deconvolution algorithm into ePIE³⁸. Therefore, all subsequent references to traditional ptychography are based on the same ePIE algorithm, using consistent numerical parameters and the same position correction method⁴¹, to ensure a fair comparison. Further details can be found in Supplementary Table 1. Here, the central wavelength of our broadband source, 706 nm, was used during the iterative retrieval process. Figure 2b shows the amplitude and phase of the ant specimen reconstructed using traditional ePIE, in which almost no distinguishable details of the ant are visible. In this reconstruction, the algorithm cannot converge due to the incorrect assumption of full coherence. By introducing the convolution model into ptychography, the estimated diffraction intensities can be progressively closer to the recorded diffraction patterns as the iterations go on, which is helpful for the convergence of the algorithm. Figure 2c shows the reconstructed structured probe and sample using our method. The probe is well reconstructed, since the backward propagation to the pinhole yields a clear USAF image as shown in the blue box of Fig. 2c. The outline and detail information of reconstructed amplitude align well with the optical microscope image. As the central wavelength of source is closer to the infrared range, offering better penetration for biological specimens, the recovered amplitude reveals clearer internal details of the ant body. After phase unwrapping with least-squares phase unwrapping method⁴², the stacked structures of the ant are also clearly revealed. To quantitatively evaluate the spatial resolution of the reconstructed image, we employed the Fourier ring correlation (FRC), a widely used criterion in ptychography^{13,15}. The resulting FRC curve of reconstructed amplitude was evaluated against the half-bit threshold⁴³ to determine the resolution. As shown in the Supplementary Fig. 2, the intersection point corresponds to a spatial resolution of $13.74 \mu\text{m}$, which closely matches the theoretical resolution of $12.73 \mu\text{m}$, determined by twice the sampling interval at the sample plane. Notably, the resolution here is determined by the system settings and adapted to the resolution requirements of samples. This marks the first successful demonstration of clear ptychographic imaging of biological structures under ultra-broadband sources, validating the effectiveness of our method for complex amplitude sample imaging. This achievement significantly alleviates the limitations of broadband algorithms in practical biological and medical applications.

Broadband quantitative phase imaging

The quantitative phase imaging (QPI) capability is one of the key advantages of ptychography over traditional lens-based imaging techniques. Therefore, it is crucial to validate the QPI capability of our ultra-broadband ptychography method. Here, a custom-designed waveform modulation plate was selected as a sample. This plate has a random binary phase pattern with a 50% fill factor, fabricated through exposure and development of AZ4562 photoresist (detailed in Methods). The pattern on the plate has a consistent thickness, ensuring a uniform phase shift at a single wavelength, which facilitates measurement of its phase value. The phase shift $\Delta\phi$ is determined by the thickness d and refractive index n of the photoresist and is given by,

$$\Delta\phi = \frac{2\pi}{\lambda} nd \quad (2)$$

where λ denotes the illumination wavelength. To obtain an accurate phase value as a reference, we first performed ptychographic imaging under narrowband illumination, which has been proven to exhibit QPI capability⁴⁴. A bandpass filter was introduced to the broadband source above, yielding a filtered central wavelength of 780 nm with a FWHM of 10 nm, resulting in a bandwidth of approximately 1%. Using this narrowband illumination, we recorded a set of diffraction data from the phase plate, while one of patterns is shown in Fig. 3a. The diffraction pattern clearly exhibits distinct speckle characteristics along with uniformly distributed random interference fringes, indicating a

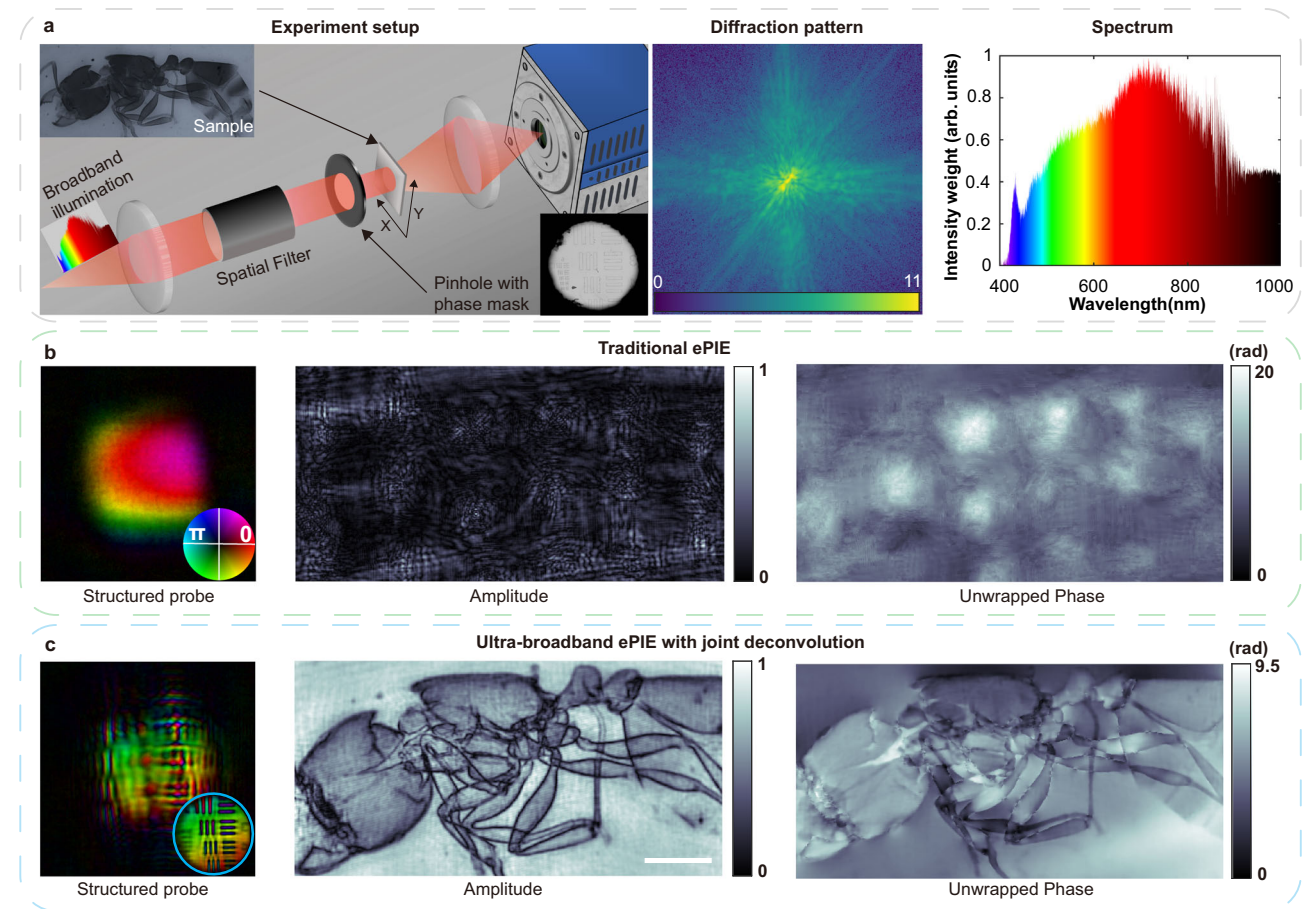


Fig. 2 | Optical biology experiment of ultra-broadband ptychography at 60% bandwidth. **a** A proof-of-concept imaging system for ultra-broadband ptychography is depicted and described. The system integrates a super-continuous light source. After collimation and spatial filtering, broadband light passes through a pinhole with a phase-type USAF resolution target to form a light probe that illuminates the ant sample. The displayed images of the sample and pinhole with phase mask were obtained by an optical microscope. Additionally, a broadband diffraction pattern displayed on a logarithmic scale is presented. The spectral distribution

of the continuum source employed for ultra-broadband illumination is also presented. **b** The reconstructed structured probe result, including the amplitude and phase of the ant specimen reconstructed using traditional ptychography, is displayed. **c** The reconstructed structured probe and sample using our ultra-broadband ptychography method are showcased. The backward propagation to the pinhole yields a clear USAF image, as indicated within the blue circle. The scale bar in (c) corresponds to 500 μ m.

high degree of coherence in the source. Figure 3b, c shows the reconstructed probe and phase with a phase offset, recovered from traditional narrowband ptychography, while the bright areas of Fig. 3c represent the patterned regions and the dark areas correspond to the blank regions. The phase region enclosed by red box of Fig. 3a was displayed in 3D in Fig. 3b, demonstrating that the randomly distributed blocks with smooth surfaces and sharp edges can be accurately reconstructed. Additionally, we plotted the phase profile along the red dashed line, and determined a phase shift of 2.49 rad at 780 nm for the binary phase plate. Rescaling the phase to 706 nm using Eq. (2) while keeping n and d constant yields a phase shift of 2.77 rad through the filled pixels of the binary structure, which we use as a reference for quantitative comparisons in the following broadband experiments.

In this work, an important improvement is the introducing of phase modulation on the illumination probe, which can enhance broadband imaging performance at higher photon throughout compared to using an absorption mask. To quantitatively analyse the impact of structured illumination on the imaging quality of ultra-broadband ptychography, we conducted comparative experiments using a binary phase plate. Both diffraction datasets using uniform or structured illumination were recorded with a 60% bandwidth source and a total photon count of 2×10^7 , identical to the narrowband case.

As shown in Fig. 3e, i, the interference fringes in the diffraction speckle patterns were both significantly blurred. The proposed ultra-broadband reconstruction algorithm was run on both datasets using identical parameters, yielding high-quality reconstructions of the probes and the pinhole structures in both cases, as shown in Fig. 3f, j. However, the reconstructed phase plate under uniform illumination exhibited significant image distortion, with a structural similarity (SSIM) of only 0.3996 calculated against the reference image shown in Fig. 3c. Figure 3h presents the 3D phase map and phase profile of the same region as in Fig. 3d, exhibiting pronounced fluctuations and noise. The calculated global phase shift is 2.85 rad, which is close to the reference value of 2.77 rad, demonstrating that our ultra-broadband ptychography can retain QPI capability under uniform illumination. With structured illumination, phase reconstruction with higher contrast was obtained (Fig. 3k), achieving an SSIM value of 0.7362. The red-boxed region of the retrieved phase is also displayed in 3D in Fig. 3l, showing similarly sharp edges, with only slight distortions at the block corners where they appear slightly rounded. Additionally, the phase profile appears overall smooth, with only minor fluctuations. The global phase shift was also calculated, yielding a value of 2.82 rad. These results demonstrate that our ultra-broadband algorithm maintains good QPI capability under both uniform and structured illumination, while structured illumination can significantly enhance the

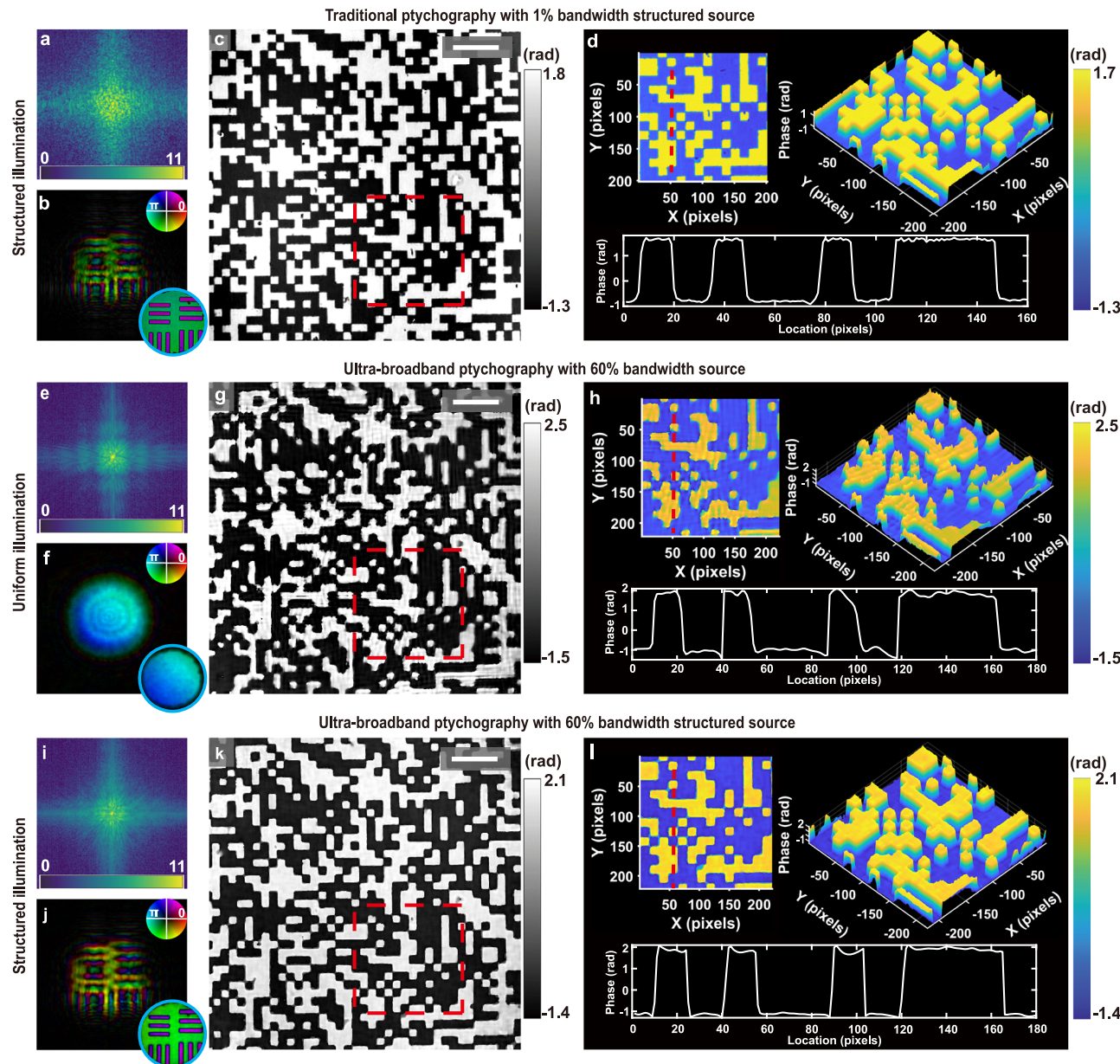


Fig. 3 | Quantitative phase analysis of the binary phase plate. **a** A far-field diffraction pattern obtained under narrowband illumination is presented, which is displayed on a logarithmic scale. **b** The reconstructed structured probe and its backward propagation to the pinhole are showcased. **c** Reconstructed phase of binary phase plate achieved from traditional ptychography with 1% bandwidth. The bright areas signify patterned regions, while the dark areas correspond to blank regions. **d** The 3D visualization of the region enclosed by the red box in (c) and the phase profile along the red dashed line. **e** The diffraction pattern obtained under 60% bandwidth uniform illumination exhibits pronounced blur. **f** The

reconstructed uniform probe and its backward propagation. **g** Reconstructed phase of the same sample using ultra-broadband ptychography shows image distortion compared to (c). **h** 3D phase map and phase profile of the same region as in (d). **i** The diffraction pattern obtained under 60% bandwidth structured illumination. **j** The reconstructed structured probe and its backward propagation. **k** Reconstructed phase using ultra-broadband ptychography exhibits similar quality to (c). **l** A 3D visualization and phase profile similar to those shown in (d). The scale bar in (c) corresponds to 280 μm and the scale bar in (g, k) correspond to 270 μm .

quality of broadband reconstructions and improve QPI accuracy. Moreover, broadband experiments using a USAF resolution target (LBTEK) showed that structured illumination improved the resolution by 14% compared to uniform illumination (details can be found in the Supplementary materials).

Performance of different broadband methods in ptychography
The aforementioned mainstream broadband methods employing numerical monochromatization have demonstrated exceptional performance in CDI²⁸, and have recently been applied to ptychography^{29,30}, further enhancing its capabilities. Therefore, we evaluated the

performance of monochromatization ptychography (monoPTY) and our proposed method using different samples under a 15% bandwidth light source, with ptychography results under 1.8% bandwidth conditions serving as the benchmark for comparison. The system used in these experiments is consistent with the setup mentioned above, with only the illumination bandwidth being adjusted by changing the filter. Here, the broadband structured illumination has a central wavelength of 550 nm and a FWHM of 80 nm, while the narrowband structured illumination has a central wavelength of 523 nm and a FWHM of 10 nm.

Figure 4 shows the reconstructed results of three samples with different characteristics under the aforementioned experimental

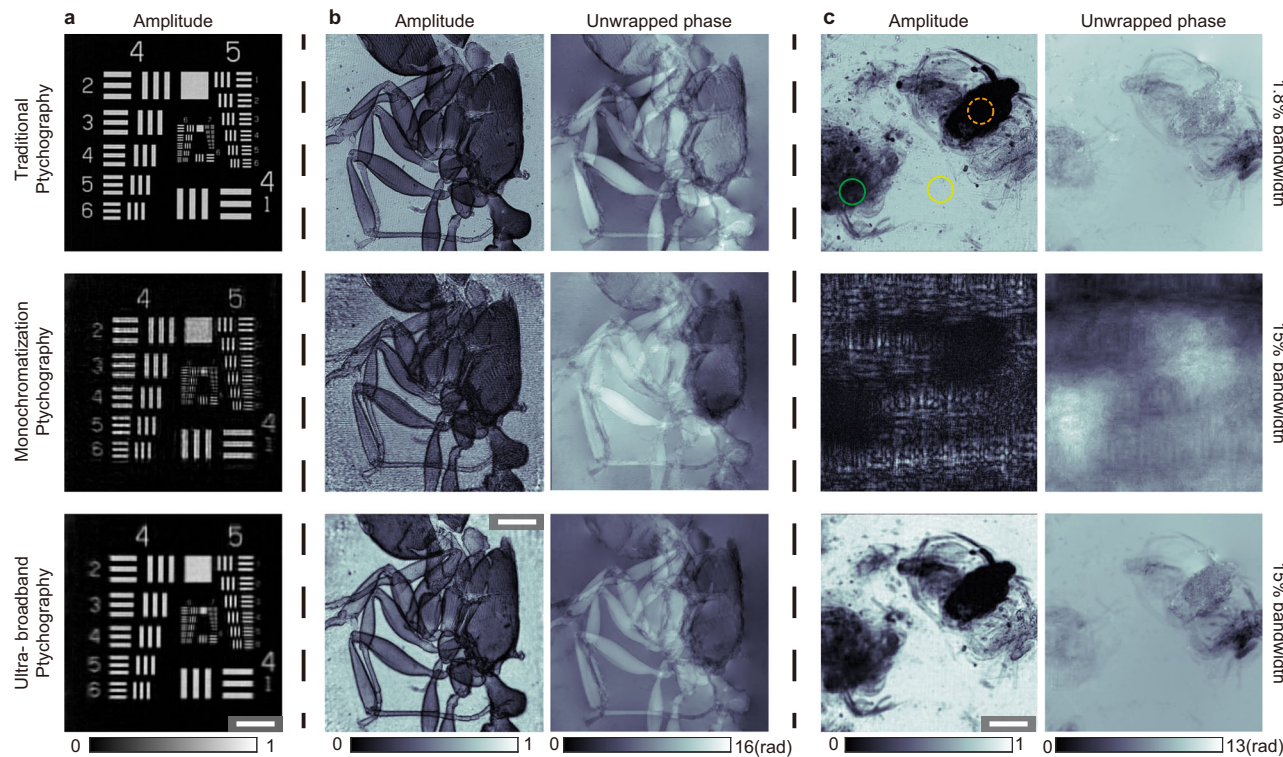


Fig. 4 | Performance of different broadband methods in ptychography experiments. The results of the 1.8% bandwidth source combined with traditional ptychography are used as the benchmark for comparison, followed by the processing and comparison of diffraction data from the 15% bandwidth source using monochromatized ptychography and ultra-broadband ptychography, respectively. **a** Reconstruction of an amplitude-type USAF resolution target. **b** Reconstruction of

an unstained ant specimen. **c** Reconstruction of a freshwater copepod sample. The yellow circle indicates an empty region, the green circle marks the Fast Green-stained sample region, and the orange dashed circle denotes the Eosin-stained sample region. The scale bar in (a) corresponds to 200 μm ; the scale bar in (b) corresponds to 300 μm and the scale bar in (c) corresponds to 400 μm .

conditions. The first row displays the reconstruction using the traditional ptychography under a 1.8% bandwidth source, and the second row and third row show the reconstruction using monoPTY and ultra-broadband ptychography respectively under a 15% bandwidth source. We first use an amplitude-type USAF resolution target as a non-dispersive sample for reconstruction testing, as shown in Fig. 4a. The results demonstrate that the 15% bandwidth diffraction data, reconstructed using both broadband algorithms, achieve a comparable image quality to that of the narrowband data. The FRC analysis yielded a spatial resolution of 8.18 μm at 532 nm narrowband illumination, which was scaled to 8.46 μm at 550 nm. In comparison, the resolution of monoPTY was 9.44 μm , corresponding to a 12% degradation, whereas the resolution of ultra-broadband ptychography was 8.74 μm , with only a 3.3% degradation. The FRC results were shown in Supplementary Fig. 3. Notably, spectral averaging inherent in broadband diffraction data suppresses high-frequency interference fringes, reduces recoverability of data under noisy conditions, and consequently leads to degraded resolution. Subsequently, we conducted a further performance comparison of the algorithm using biological samples. Figure 4b presents a comparison of image reconstruction for the unstained ant specimen. The narrowband ptychography reconstructs the amplitude information of the ant sample with high clarity achieving a resolution of 8.37 μm , and the unwrapped phase clearly reveals its internal structural details. In contrast, the reconstruction amplitude of monoPTY exhibits high background noise, with the resolution degrading to 9.51 μm . This is primarily due to the deviation of the ant sample from the non-dispersive assumption, where the far-field diffraction patterns of different wavelengths are no longer simply related through direct scaling. Indeed, our method overcomes this limitation due to its different broadband model construction,

reconstructing high-quality images with low background noise and a resolution of 8.82 μm close to that of narrowband ptychography.

Accurate spectral information is an essential prior knowledge for monoPTY, typically obtained directly through a spectrometer. Although recent work has enabled the direct retrieval of the spectral distribution of the illumination after transmission through the sample for numerical monochromatization³⁰, this approach is applicable only to nondispersive samples or samples with globally invariant absorption characteristics. However, most samples consist of multiple materials with different absorption characteristics, leading to significant variations in the transmitted spectrum across different scanning regions, making it evidently challenging for methods that rely on precise spectral distribution to image such samples. The absorption edges of elements are primarily concentrated in the shorter wavelength region, particularly in the X-ray and EUV ranges. Therefore, we selected a stained freshwater copepod, which is a standard biological section (SAGA) obtained by regionally staining with Fast Green and Eosin, to simulate absorption edge effects in the visible light spectrum regime. In Fig. 4c, the transmitted spectrum from the blank region (yellow circle) corresponds to the source spectrum, which is relatively uniform across the 500–600 nm range. The transmitted spectrum from the Fast Green-stained region (green solid circle) exhibits a sharp decline near 600 nm, whereas that from the Eosin-stained region (orange dashed circle) drops steeply near 500 nm, demonstrating clear absorption differences. The color image of the sample, three distinct transmitted spectral distributions and two reconstructions using narrowband ptychography at two different wavelengths, can be found in Supplementary Fig. 4. Here, monoPTY processes the diffraction data using the spectral prior information of source and the results reveal only blurred contours, with all other information

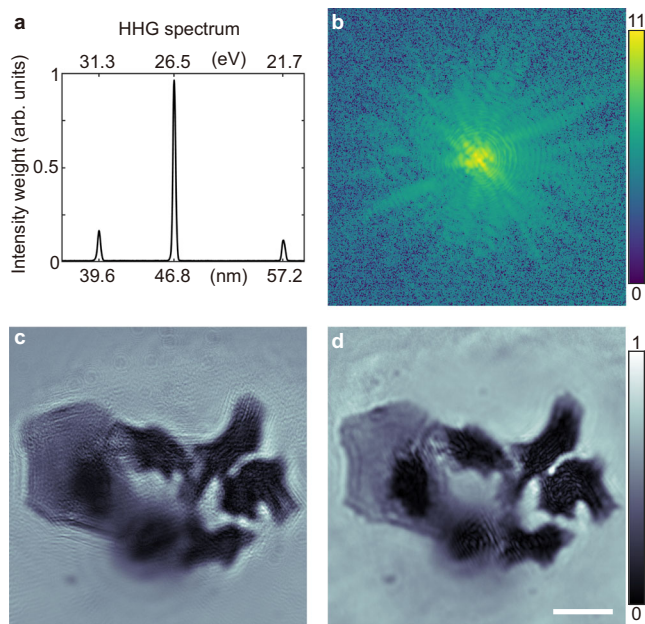


Fig. 5 | EUV experimental validation using tabletop HHG source. **a** The spectrum of an EUV HHG source. **b** Polychromatic diffraction pattern obtained by the source. **c** Reconstructed amplitude of osteosarcoma cells using traditional ePIE. **d** Reconstructed amplitude of the same sample using ultra-broadband ePIE. The scale bar in **(d)** corresponds to 25 μm .

completely lost. This further demonstrates that the spectral response of the sample can significantly impact the reconstruction quality of methods that rely on spectral priors. Moreover, we also attempted to incorporate the transmitted spectrum of the sample as prior information in the monoPTY reconstruction (Supplementary Fig. 5). However, no improvement was observed compared to using the source spectrum, primarily due to the inability to perform spectral detection or calibration at each scanning position in ptychography. In contrast, the reconstructed amplitude and unwrapped phase using ultra-broadband ptychography still exhibit high image quality and high resolution (9 μm) comparable to that achieved under the narrowband source (8.8 μm at 550 nm). This performance benefits from our joint deconvolution method, which progressively decouples the blur kernels containing coherence information from the diffraction data during the iterative process. Notably, each diffraction pattern is associated with an individual kernel. Through this broadband visible-light experiment, we successfully demonstrated that the proposed ultra-broadband ptychography can achieve high-quality reconstructions even for samples exhibiting absorption edge effects. Moreover, we also evaluated mixed-state method² for comparison as shown in Supplementary Fig. 6, which has been demonstrated to be robust to broadband illumination⁴⁰. This comparison illustrates the strength of our method in providing robust imaging performance for dispersive samples under broadband illumination. Therefore, our proposed method holds strong potential for practical application to the imaging of mixed materials using HHG EUV or broadband X-ray sources.

Broadband ptychography with HHG EUV source

While synchrotron facilities have long served as the dominant sources for X-ray ptychography due to their high brightness and coherence, their limited accessibility and infrastructural demands constrain broader experimental deployment. Therefore, the combination of broadband laboratory-scale EUV or X-ray sources with ptychography offers a promising route to mitigate these limitations and enable more accessible high-resolution imaging. To evaluate the applicability of our ultra-broadband ptychography for broadband laboratory-scale

sources, we further conducted a validation experiment using a tabletop EUV source whose spectrum containing three harmonics as shown in Fig. 5a. The restricted wavelength range (40–57 nm) makes it difficult to obtain suitable absorption-edge samples. Consequently, biological specimens, which are readily available and easy to prepare, were employed to demonstrate that the proposed method can effectively enhance reconstruction quality under discrete broadband EUV. Considering the resolution capability of the experimental system, we ultimately selected osteosarcoma cells as the sample, mounted on a 50-nm-thick silicon nitride membrane as the supporting substrate. Figure 5b shows the acquired multichromatic diffraction pattern. Here, in comparison with reconstruction of traditional ePIE (Fig. 5c), a significant improvement in the reconstruction quality of osteosarcoma cells can be observed using ultra-broadband ePIE (Fig. 5d). Furthermore, the achievable resolution was enhanced from 776 nm to 640 nm, corresponding to an improvement of approximately 18%. We also compared the results using the polychromatic ePIE from the previous work⁴⁵, and found that the ultra-broadband ptychography still provides superior image quality (Supplementary Fig. 6). This is because the polychromatic method in ref. 45 is also primarily based on the assumption of non-dispersive samples. Notably, due to the high absorption of the biological sample in the utilized wavelength range, only the contour information is clearly revealed. Therefore, this experiment serves solely as an attempt to demonstrate the applicability of this method for imaging dispersive samples using broadband tabletop EUV sources (Experimental details in Methods).

Discussion

We have demonstrated a practical solution to the challenges of broadband imaging in dispersive samples, which is, in principle, applicable to broadband sources across any wavelength range and to samples with varying spectral responses. The ultra-broadband ptychography overcomes several challenges associated with traditional broadband methods. Our method incorporates the convolution model to address the issue where broadband far-field diffraction patterns of dispersive samples cannot be accurately fitted through wavelength scaling. Additionally, we demonstrate that this method enables high-quality imaging without any prior spectral knowledge or the sample spectral response, effectively overcoming the significant challenges of traditional broadband methods when samples exhibit regionally varying spectral responses. Furthermore, we introduced a phase mask into the system to enable structured illumination, significantly enhancing reconstruction quality while minimizing energy loss. As an algorithmic innovation, we combine the iterative blind deconvolution algorithm with the multi-kernel strategy in ultra-broadband ePIE, leveraging data redundancy to solve the mutual coherence functions at each scan position. We have presented biological sample imaging under an ultra-broadband source with a 60% bandwidth and demonstrated the quantitative phase imaging capability of the proposed method. Moreover, by simulating absorption edge effects using a biological sample stained with different staining agents in the visible range, the results further demonstrate the substantial advantages of ultra-broadband ptychography over other broadband methods. The HHG EUV biological imaging experiment further demonstrates that our method maintains robust performance when extended to short-wavelength sources.

The broadband imaging capability of ultra-broadband ptychography can potentially become a critical asset in addressing the flux limitations of laboratory-scale X-ray sources caused by monochromatic filtering. The combination of broadband diffraction imaging techniques with the high brightness of laboratory-scale broadband X-ray sources presents a promising method for transitioning biological and material analysis from large-scale facilities to laboratory settings. On one hand, it is complementary to current efforts to enhance the flux of existing laboratory-scale X-ray imaging systems to improve

reconstruction quality under dose-limited conditions. On the other hand, the proposed method is applicable to dispersive samples and is expected to enable element-specific imaging with further algorithmic development.

Methods

Details of optical experiments

In our optical experiments, a broadband illumination centered at about 706 nm with 60% bandwidth was used as the source. Here, a 4 f system is used to perform aperture filtering on the illumination, thereby enhancing its spatial coherence. A 600 μm pinhole serves as an aperture to confine the illumination size, thereby ensuring that the probe generated at the sample plane satisfies the oversampling criterion⁴⁶. All samples are placed on a stepper motor stage (Newport MFA-CC) and scanned relative to the probe following a scan pattern with a concentric trajectory, with a step size of 70 μm between adjacent positions. Subsequently, the detector (ZL41 Wave, Andor), with pixels 6.5 μm in size, recorded a series of broadband diffraction patterns, each of size 512 \times 512 pixels, for phase retrieval. The far-field diffraction data is obtained after the exit wave of sample propagates through an achromatic Fourier lens with a 30-mm focal length.

Details of EUV experiments

In the EUV experiments, the tabletop HHG source uses a commercial femtosecond laser (Light Conversion, Pharos) with a central wavelength of 1030 nm as the driving source. The laser beam is focused to 5 mm and passed through a 0.5 mm BBO crystal, generating laser pulses with a central wavelength of 515 nm, an average power of 1.8 W, and a pulse duration of 180 fs. Then, the 515 nm beam is focused into a 95-mbar pressurized Argon gas cell with a focal spot size of 60 μm , where the gas cell is a tube with an inner diameter of 2 mm. Finally, a 250 nm thick Al filter is used to remove the driving laser, yielding a pure HHG beam. More detailed information about this HHG source can be found in ref. 45. The beam containing three harmonic components is focused by a toroidal mirror onto a 20- μm pinhole to form the probe. Subsequently, the sample mounted on a translation stage (LS35.Lab.O, MultiFields Tech) is scanned with a step size of 3 μm . The exit waves propagate freely over 37 mm and are captured by a detector (XF95, Tucsen) with an 11 μm pixel size, producing polychromatic diffraction patterns with 512 \times 512 pixels.

Fabrication of binary phase plate

A substrate was first prepared for the mask fabrication. In this case, after ensuring its surface cleanliness and smoothness, a layer of AZ4562 photoresist was spin-coated onto the substrate. The photoresist, which mainly consists of phenolic resin, photoinitiator, plasticizer, and solvent, was then exposed to ultraviolet (UV) light through a pre-designed photomask. The photomask was designed with a specific binarized random pattern, which was defined by a digital layout consisting of 1000 \times 1000 pixels with a pitch of 50 μm . Based on the characteristics of the photoresist and the desired pattern features, the exposure dose and development time are optimized. Through iterative fabrication and subsequent inspection, the desired pattern depth on the substrate is ultimately achieved.

Broadband convolution model

In far-field ptychography, the Fraunhofer diffraction patterns of exit waves $\phi_j(\mathbf{r}) = P(\mathbf{r})O(\mathbf{r} + \mathbf{r}_j)$ can be expressed as,

$$I_j^{coh}(\mathbf{q}) = |\psi_j(\mathbf{q})|^2 = \left| \int P(\mathbf{r})O(\mathbf{r} + \mathbf{r}_j)e^{-i\mathbf{q}\cdot\mathbf{r}} d\mathbf{r} \right|^2 \quad (3)$$

where ψ_j is the Fourier transform of ϕ_j , $O(\mathbf{r} + \mathbf{r}_j)$ is the object transmission function, $P(\mathbf{r})$ is the probe function and \mathbf{r} is a position vector in the sample plane. This represents the diffraction intensity under ideal

conditions of full coherence. When the imaging system experiences decoherence effects due to partial coherent illumination, sample motion, or detector point spread, additional parameters must be introduced into Eq. (3) to characterize the degree of coherence, thereby obtaining an expression for partially coherent diffraction intensity I_j^{coh} ,

$$I_j^{coh}(\mathbf{q}) = \iint J(\mathbf{r}_1, \mathbf{r}_2) \gamma_{||}(\mathbf{r}_1 - \mathbf{r}_2) O^*(\mathbf{r}_1 + \mathbf{r}_j) O(\mathbf{r}_2 + \mathbf{r}_j) e^{-i\mathbf{q}\cdot(\mathbf{r}_1 - \mathbf{r}_2)} d\mathbf{r}_1 d\mathbf{r}_2 \quad (4)$$

where $J(\mathbf{r}_1, \mathbf{r}_2)$ represents the mutual optical intensity (MOI) and $\gamma_{||}(\mathbf{r}_1 - \mathbf{r}_2)$ captures the temporal (or longitudinal) coherence properties associated with the spectral bandwidth of the illumination. According to the generalized Schell model, the MOI can be further described as $J(\mathbf{r}_1, \mathbf{r}_2) = P(\mathbf{r}_1)P^*(\mathbf{r}_2)\gamma_{\perp}(\mathbf{r}_1 - \mathbf{r}_2)$, where $\gamma_{\perp}(\mathbf{r}_1 - \mathbf{r}_2)$ represents the spatial (or transverse) coherence properties. Therefore, the impact of partial coherence can be effectively described using the normalized mutual coherence function (MCF), which is defined as $\gamma = \gamma_{\perp}\gamma_{||}$. By simplifying Eq. (4), the blurred diffraction pattern resulting from partial coherence can ultimately be expressed using a convolution model^{33,34}

$$I_j^{coh}(\mathbf{q}) = I_j^m(\mathbf{q}) \otimes \hat{\gamma}_j(\mathbf{q}) \quad (5)$$

where $\hat{\gamma}_j(\mathbf{q})$ is the Fourier transform of the normalized MCF. Incorporating this diffraction intensity model into the ptychography reconstruction algorithm allows for a more accurate representation of the measured broadband diffraction data.

However, the MCF of system cannot be easily pre-calibrated for dispersive samples. Therefore, a critical step in the reconstruction algorithm of ultra-broadband ptychography is solving for the kernel $\hat{\gamma}_j(\mathbf{q})$ that contains partial coherence information. We integrated the Wiener-Lucy (W-L) tandem deconvolution algorithm with ePIE to develop a blur-kernel-decoupling method (joint deconvolution), which fully exploits the data redundancy inherent in ptychography to enhance the accuracy of the deconvolution. Considering the relatively consistent overall coherence of the system, the kernels corresponding to different diffraction patterns are expected to exhibit substantial similarity. Thus, the kernel solved from the previous scan position is used as the initial value in the current deconvolution iteration, significantly enhancing the speed and accuracy of $\hat{\gamma}_j(\mathbf{q})$ decoupling. The iterative decoupling process of $\hat{\gamma}_j(\mathbf{q})$ is given by,

$$\begin{aligned} \hat{\gamma}_{k+1,j}(\mathbf{q}) &= \omega_1 \hat{\gamma}_{k,j}(\mathbf{q}) \left[\frac{I_j^m(\mathbf{q})}{I_j^{coh}(\mathbf{q}) \otimes \hat{\gamma}_{k,j}(\mathbf{q})} \otimes I_j^{coh}(\mathbf{q}) \right] \\ &\quad + \omega_2 \mathcal{F}^{-1} \left[\frac{\text{conj}[\mathcal{F}(I_j^{coh}(\mathbf{q}))]}{\left| \mathcal{F}(I_j^{coh}(\mathbf{q})) \right|^2} \mathcal{F}(I_j^m(\mathbf{q})) \right], \end{aligned} \quad (6)$$

where \mathcal{F} represents the Fourier transform operator, ‘conj’ denotes the complex conjugate operation and k represents the sub-iteration index which is set to 20 iterations. $I_j^m(\mathbf{q})$ is the measured diffraction data. ω_1 and ω_2 are weighted coefficients summing to 1, with ω_1 gradually increasing and ω_2 decreasing as the sub-iterations progress. Notably, $\hat{\gamma}_{k=0,j}(\mathbf{q}) = \hat{\gamma}_{j-1}(\mathbf{q})$. After more than half of the algorithm iterations, we remove the associations above between the blur kernels, allowing them to update independently. This operation compensates for spectral variations at each scan position or disturbances caused by light source jitter, thereby significantly improving the reconstruction quality of the image.

Reconstruction algorithm

Ultra-broadband ptychography primarily incorporates a convolution model into traditional ptychography to represent broadband

diffraction patterns, while employing a blind deconvolution approach to simultaneously separate fully coherent diffraction patterns and the blur kernel during the iterative process. Normally, we start with the estimated exit waves of sample $\varphi_{i,j}(\mathbf{r}) = P(\mathbf{r}_i)O(\mathbf{r}_i + \mathbf{r}_j)$ and proceed as follows for the i th iteration,

- Propagating $\varphi_{i,j}(\mathbf{r})$ to the detector plane generates an estimate of the fully coherent diffraction intensity $I_{i,j}^{coh}(\mathbf{q})$ as shown in Eq. (3).
 - Applying the iterative blind deconvolution algorithm yields the estimate of FT-MCF,
- $$\hat{\gamma}_{i,j}(\mathbf{q}) = deconvWL\left\{I_{i,j}^m(\mathbf{q}), I_{i,j}^{coh}(\mathbf{q}), \hat{\gamma}_{i,j-1}(\mathbf{q})\right\} \quad (7)$$
- where $deconvWL\{\cdot\}$ represents the W-L tandem deconvolution algorithm. Every 10 iterations in the paper, the $\hat{\gamma}_j(\mathbf{q})$ will be updated.
- Generate the estimate of broadband diffraction pattern $I_{i,j}^{pcoh}(\mathbf{q})$ according to Eq. (5).
 - Apply the modulus constraint to $\psi_{i,j}(\mathbf{q})$,

$$\hat{\psi}_{i,j}(\mathbf{q}) = \psi_{i,j}(\mathbf{q}) \left[\frac{\sqrt{I_{i,j}^m(\mathbf{q})}}{\sqrt{I_{i,j}^{pcoh}(\mathbf{q})}} \right] \quad (8)$$

- Back-propagate $\hat{\psi}_{i,j}(\mathbf{q})$ to the sample plane to form a revised exit wave $\hat{\varphi}_{i,j}(\mathbf{r})$. Subsequently, apply the overlap constraint to update both the object and probe simultaneously according to the following functions:

$$\hat{O}(\mathbf{r}_i + \mathbf{r}_j) = O(\mathbf{r}_i + \mathbf{r}_j) + \alpha \frac{\text{conj}(P(\mathbf{r}_i)) [\hat{\varphi}_{i,j}(\mathbf{r}) - \varphi_{i,j}(\mathbf{r})]}{|P(\mathbf{r}_i)|_{\max}^2} \quad (9)$$

$$\hat{P}(\mathbf{r}_i) = P(\mathbf{r}_i) + \alpha \frac{\text{conj}(O(\mathbf{r}_i + \mathbf{r}_j)) [\hat{\varphi}_{i,j}(\mathbf{r}) - \varphi_{i,j}(\mathbf{r})]}{|O(\mathbf{r}_i + \mathbf{r}_j)|_{\max}^2} \quad (10)$$

where the coefficient α , a constant set to a value of 1 in our experiment, could affect the convergence speed and robustness of the phase retrieval algorithm.

Repeat the above steps until all positions have been updated to complete one iteration. The reconstruction process will terminate after a predetermined number of iterations.

Data availability

The data that support the findings of this study are available from the corresponding author upon request.

Code availability

Codes used to post-process the diffraction data within this paper are available from the corresponding author upon request.

References

- Chapman, H. N. & Nugent, K. A. Coherent lensless X-ray imaging. *Nat. Photon.* **4**, 833–839 (2010).
- Thibault, P. & Menzel, A. Reconstructing state mixtures from diffraction measurements. *Nature* **494**, 68–71 (2013).
- Pfeiffer, F. X-ray ptychography. *Nat. Photon.* **12**, 9–17 (2018).
- Rodenburg, J. M. & Faulkner, H. M. L. A phase retrieval algorithm for shifting illumination. *Appl. Phys. Lett.* **85**, 4795–4797 (2004).
- Thibault, P. et al. High-Resolution Scanning X-ray Diffraction Microscopy. *Science* **321**, 379–382 (2008).
- Dierolf, M. et al. Ptychographic X-ray computed tomography at the nanoscale. *Nature* **467**, 436–439 (2010).
- Maiden, A. M., Morrison, G. R., Kaulich, B., Gianoncelli, A. & Rodenburg, J. M. Soft X-ray spectromicroscopy using ptychography with randomly phased illumination. *Nat. Commun.* **4**, 1669 (2013).
- Shapiro, D. A. et al. Chemical composition mapping with nanometre resolution by soft X-ray microscopy. *Nat. Photon.* **8**, 765–769 (2014).
- Holler, M. et al. High-resolution non-destructive three-dimensional imaging of integrated circuits. *Nature* **543**, 402–406 (2017).
- Aidukas, T. et al. High-performance 4-nm-resolution X-ray tomography using burst ptychography. *Nature* **632**, 81–88 (2024).
- Batey, D. J. et al. X-Ray Ptychography with a Laboratory Source. *Phys. Rev. Lett.* **126**, 193902 (2021).
- Gardner, D. F. et al. Subwavelength coherent imaging of periodic samples using a 13.5 nm tabletop high-harmonic light source. *Nat. Photon.* **11**, 259–263 (2017).
- Baksh, P. D. et al. Quantitative and correlative extreme ultraviolet coherent imaging of mouse hippocampal neurons at high resolution. *Sci. Adv.* **6**, eaaz3025 (2020).
- Tanksalvala, M. et al. Nondestructive, high-resolution, chemically specific 3D nanostructure characterization using phase-sensitive EUV imaging reflectometry. *Sci. Adv.* **7**, eabd9667 (2021).
- Eschen, W. et al. Material-specific high-resolution table-top extreme ultraviolet microscopy. *Light Sci. Appl.* **11**, 117 (2022).
- Liu, C. et al. Visualizing the ultra-structure of microorganisms using table-top extreme ultraviolet imaging. *PhotonX* **4**, 6 (2023).
- Xu, W., Ning, S. & Zhang, F. Numerical and experimental study of partial coherence for near-field and far-field ptychography. *Opt. Express* **29**, 40652 (2021).
- Schropp, A. & Schroer, C. G. Dose requirements for resolving a given feature in an object by coherent x-ray diffraction imaging. *N. J. Phys.* **12**, 035016 (2010).
- Thibault, P., Guizar-Sicairos, M. & Menzel, A. Coherent imaging at the diffraction limit. *J. Synchrotron Rad.* **21**, 1011–1018 (2014).
- Chen, B. et al. Multiple wavelength diffractive imaging. *Phys. Rev. A* **79**, 023809 (2009).
- Abbey, B. et al. Lensless imaging using broadband X-ray sources. *Nat. Photon.* **5**, 420–424 (2011).
- Batey, D. J., Claus, D. & Rodenburg, J. M. Information multiplexing in ptychography. *Ultramicroscopy* **138**, 13–21 (2014).
- Zhang, B. et al. Ptychographic hyperspectral spectromicroscopy with an extreme ultraviolet high harmonic comb. *Opt. Express* **24**, 18745 (2016).
- Rana, A. et al. Potential of Attosecond Coherent Diffractive Imaging. *Phys. Rev. Lett.* **125**, 086101 (2020).
- Yao, Y. et al. Broadband X-ray ptychography using multi-wavelength algorithm. *J. Synchrotron Rad.* **28**, 309–317 (2021).
- Shao, Y. et al. Wavelength-multiplexed multi-mode EUV reflection ptychography based on automatic differentiation. *Light Sci. Appl.* **13**, 196 (2024).
- Dilanian, R. A. et al. Diffractive imaging using a polychromatic high-harmonic generation soft-x-ray source. *J. Appl. Phys.* **106**, 023110 (2009).
- Huijts, J. et al. Broadband coherent diffractive imaging. *Nat. Photon.* **14**, 618–622 (2020).
- Liu, R. et al. Broadband ptychographic imaging with an accurately sampled spectrum. *Phys. Rev. A* **107**, 033510 (2023).
- Chen, C., Gu, H. & Liu, S. Ultra-broadband diffractive imaging with unknown probe spectrum. *Light Sci. Appl.* **13**, 213 (2024).
- Li, B. et al. Snapshot coherent diffraction imaging across ultra-broadband spectra. *Photon. Res.* **12**, 2068 (2024).
- Wolf, E. New theory of partial coherence in the space-frequency domain Part I: spectra and cross spectra of steady-state sources. *J. Opt. Soc. Am.* **72**, 343 (1982).

33. Vartanyants, I. A. & Robinson, I. K. Partial coherence effects on the imaging of small crystals using coherent x-ray diffraction. *J. Phys.: Condens. Matter* **13**, 10593–10611 (2001).
34. Nugent, K. A. Coherent methods in the X-ray sciences. *Adv. Phys.* **59**, 1–99 (2010).
35. Clark, J. N. & Peele, A. G. Simultaneous sample and spatial coherence characterisation using diffractive imaging. *Appl. Phys. Lett.* **99**, 154103 (2011).
36. Clark, J. N., Huang, X., Harder, R. & Robinson, I. K. High-resolution three-dimensional partially coherent diffraction imaging. *Nat. Commun.* **3**, 993 (2012).
37. Lin, H., Xu, W., Zhao, J. & Zhang, F. Broadband coherent modulation imaging with no knowledge of the illumination spectrum distribution. *Opt. Lett.* **48**, 3977 (2023).
38. Maiden, A. M. & Rodenburg, J. M. An improved ptychographical phase retrieval algorithm for diffractive imaging. *Ultramicroscopy* **109**, 1256–1262 (2009).
39. Loetgering, L. et al. Tailoring spatial entropy in extreme ultraviolet focused beams for multispectral ptychography. *Optica* **8**, 130 (2021).
40. Xu, W. et al. A high-performance reconstruction method for partially coherent ptychography. *Ultramicroscopy* **267**, 114068 (2024).
41. Zhang, F. et al. Translation position determination in ptychographic coherent diffraction imaging. *Opt. Express* **21**, 13592 (2013).
42. Ghiglia, D. C. & Romero, L. A. Robust two-dimensional weighted and unweighted phase unwrapping that uses fast transforms and iterative methods. *J. Opt. Soc. Am. A* **11**, 107 (1994).
43. Van Heel, M. & Schatz, M. Fourier shell correlation threshold criteria. *J. Struct. Biol.* **151**, 250–262 (2005).
44. Rodenburg, J. M. Ptychography and related diffractive imaging methods. *Adv. Imaging Electron Phys.* **150**, 87–184 (2008).
45. Li, K. et al. Tabletop ptychographic imaging system with a 515 nm laser driven high-order harmonic source. *Opt. Lasers Eng.* **176**, 108105 (2024).
46. Miao, J., Ishikawa, T., Anderson, E. H. & Hodgson, K. O. Phase retrieval of diffraction patterns from noncrystalline samples using the oversampling method. *Phys. Rev. B* **67**, 174104 (2003).

Acknowledgements

We acknowledge funding for this work from the National Natural Science Foundation of China No. 12074167 (awarded to F.Z.) and the Shenzhen Science and Technology Innovation Program No. JCYJ20241202125334045 (awarded to F.Z.). This work was supported by Center for Computational Science and Engineering at Southern University of Science and Technology. We appreciate Prof. Manuel Guizar-Sicairos (Paul Scherrer Institut, École polytechnique fédérale de Lausanne) and Dr. Abraham Lewis Levitan (Paul Scherrer Institut) for helpful suggestions on the revision of the manuscript. We thank Mr. Jianfeng You for fabricating the binary phase plate.

Author contributions

H.L. and F.Z. proposed the concept. F.Z. supervised this project; H.L. and W.X. designed the experiment system and H.L. conducted the visible light experiments reported in this paper; K.L., J.N., J.L., X.Z. and H.L. performed the tabletop EUV experiments; H.L. developed the reconstruction method and conducted image reconstruction and analyzed the data with A.L. and X.J.; H.L. conducted the data visualization with assistance from A.L. and T.L; H.L. and F.Z. wrote the manuscript and Supplementary Materials; H.L., W.X. and F.Z. were responsible for major revisions and optimizations of the manuscript.

Competing interests

The authors declare no competing interests.

Additional information

Supplementary information The online version contains supplementary material available at <https://doi.org/10.1038/s41467-025-61339-3>.

Correspondence and requests for materials should be addressed to Fucai Zhang.

Peer review information *Nature Communications* thanks Julius Huijts and the other, anonymous, reviewer(s) for their contribution to the peer review of this work. A peer review file is available.

Reprints and permissions information is available at <http://www.nature.com/reprints>

Publisher's note Springer Nature remains neutral with regard to jurisdictional claims in published maps and institutional affiliations.

Open Access This article is licensed under a Creative Commons Attribution-NonCommercial-NoDerivatives 4.0 International License, which permits any non-commercial use, sharing, distribution and reproduction in any medium or format, as long as you give appropriate credit to the original author(s) and the source, provide a link to the Creative Commons licence, and indicate if you modified the licensed material. You do not have permission under this licence to share adapted material derived from this article or parts of it. The images or other third party material in this article are included in the article's Creative Commons licence, unless indicated otherwise in a credit line to the material. If material is not included in the article's Creative Commons licence and your intended use is not permitted by statutory regulation or exceeds the permitted use, you will need to obtain permission directly from the copyright holder. To view a copy of this licence, visit <http://creativecommons.org/licenses/by-nc-nd/4.0/>.

© The Author(s) 2025